Soliton Interferometry with Very Narrow Barriers Obtained from Spatially Dependent Dressed States

Callum L. Grimshaw,[1] Thomas P. Billam,[2] and Simon A. Gardiner[1]
[1]Joint Quantum Centre (JQC) Durham–Newcastle, Department of Physics, Durham University, Durham DH1 3LE, United Kingdom
[2]Joint Quantum Centre (JQC) Durham–Newcastle, School of Mathematics, Statistics and Physics, Newcastle University, Newcastle upon Tyne NE1 7RU, United Kingdom

(Received 23 April 2021; accepted 23 May 2022; published 19 July 2022)

Bright solitons in atomic Bose-Einstein condensates are strong candidates for high precision matter-wave interferometry, as their inherent stability against dispersion supports long interrogation times. An analog to a beam splitter is then a narrow potential barrier. A very narrow barrier is desirable for interferometric purposes, but in a typical realization using a blue-detuned optical dipole potential, the width is limited by the laser wavelength. We investigate a soliton interferometry scheme using the geometric scalar potential experienced by atoms in a spatially dependent dark state to overcome this limit. We propose a possible implementation and numerically probe the effects of deviations from the ideal configuration.

DOI: 10.1103/PhysRevLett.129.040401

Bright solitons are well known within one-dimensional mean-field models of elongated attractively interacting Bose-Einstein condensates (BECs). They have been realized [1–6] in BECs of several species [7], and have much-discussed potential for atomic interferometry [8–17], owing to long interrogation times enabled by their self-support against dispersion, and the phase sensitivity of soliton collisions [18]. In the limit of high collisional velocity, and a barrier narrow relative to the soliton width, a single incident soliton can be split into two solitons with well-defined relative phase [10–12]. Under the same conditions two solitons colliding "head-on" at a barrier recombine with output populations dependent on the incident solitons' relative phase [10,11]. These processes have recently been investigated experimentally [19]; in a typical setup, focused blue-detuned laser beams realize barriers on the micron scale, comparable to a typical soliton width [19,20]. A known method to produce subwavelength features is via rapid change over a small region of the amplitude of one of two near-resonant laser fields in an atomic Λ configuration, which can be understood in terms of effective potentials experienced by spatially dependent dressed states [21–29]. We propose a technique exploiting these properties to create a single narrow barrier for soliton interferometry within a quasi-one-dimensional (quasi-1D) BEC. We subject our proposal to detailed numerical analysis of both the full Λ system and an effective single-state model, showing it to provide potentially excellent interferometric performance within an experimentally reasonable regime.

We require three internal (hyperfine) atomic states, labeled $|g_1\rangle$, $|g_2\rangle$, and $|e\rangle$ in order of increasing energy, coupled in a Λ configuration. Assuming the rotating wave approximation, we consider on-resonant laser couplings within a frame rotating with the optical frequencies, and neglect spontaneous decay from $|e\rangle$. The appropriate quasi-1D vector Gross-Pitaevskii equation (GPE) for a BEC of N mass m atoms, transversely confined by a tight harmonic trapping potential of angular frequency ω_r, is then

$$i\hbar\frac{\partial\psi_j}{\partial t} = -\frac{\hbar^2}{2m}\frac{\partial^2\psi_j}{\partial x^2} + \sum_k\left(g_{jk}^{1\mathrm{D}}|\psi_k|^2\psi_j + \frac{\hbar\Omega_{jk}}{2}\psi_k\right), \quad (1)$$

where $j,k \in \{g_1, g_2, e\}$, $g_{jk}^{1\mathrm{D}} = 2\hbar\omega_r a_{jk}$, the probe beam Rabi frequency $\Omega_{1e} = \Omega_{e1} = \Omega'(x)$, the control beam Rabi frequency $\Omega_{2e} = \Omega_{e2} = \Omega_c(x)$, and all other $\Omega_{jk} = 0$. The spatially dependent coupling means the matrix formed from Ω_{jk} elements is diagonalized by a spatially dependent dressed-state basis. Transforming to this internal-atomic-state basis produces an artificial gauge field term [21–24], resulting in a geometric scalar potential

$$V(x) = \frac{\hbar^2}{2m}\left(\frac{\Omega'\partial_x\Omega_c - \Omega_c\partial_x\Omega'}{\Omega'^2 + \Omega_c^2}\right)^2 \quad (2)$$

for atoms in the dark state $|d\rangle \propto \Omega_c(x)|g_1\rangle - \Omega'(x)|g_2\rangle$. We illustrate our scheme, using equal-width zeroth- and first-order Hermite-Gaussian modes for the probe and control beams, respectively, in Fig. 1. We express the Rabi frequencies as $\Omega'(x) = \Omega_0 l^{1/2}\phi_0(x)$ and $\Omega_c(x) = \Omega_1 l^{1/2}\phi_1(x)$, where $\phi_0(x) = [2/(\pi^{1/2}l)]^{1/2}\exp(-x^2/l^2)$ and $\phi_1(x) = (2x/l)\phi_0(x)$ are normalized Hermite-Gaussian functions of width l. Crucially, $\Omega_c(x) = h(x)\Omega'(x)$, where $h(x) = x/w$ and $w = (l/2)(\Omega_0/\Omega_1)$. In physical terms, $w = (\delta l/2)(P_0/P_1)^{1/2}$, where δ is the ($\simeq$1) ratio between dipole transition matrix elements, and P_n the nth-order

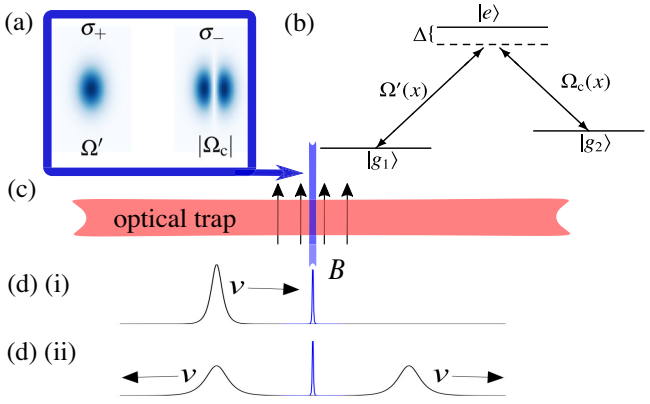

FIG. 1. Proposed coherent soliton splitting scheme. (a) Profiles of differently polarized Ω' and Ω_c barrier-forming beams in the x, z plane at $y = 0$. (b) Atomic level configuration; we typically consider $\Delta = 0$. (c) Schematic of an optical waveguide used to contain the solitons; a magnetic bias field $\boldsymbol{B}$ parallel to the Ω' and Ω_c beams provides a quantization axis. (d)(i) An initial velocity v soliton propagating in the $+x$ direction (d)(ii) splits into two equal-size counterpropagating solitons.

Hermite-Gaussian beam power. The common envelope function then cancels in the resulting dark state $|d\rangle = [|g_1\rangle - (w/x)|g_2\rangle]/[1 + (w/x)^2]^{1/2}$ and [via Eq. (2)] the geometric scalar potential

$$V_h(x) = \frac{\hbar^2}{2mw^2}\frac{1}{[1+(x/w)^2]^2}. \tag{3}$$

Phase-locking of the two laser beams is critical (to avoid population of bright states) when $|g_2\rangle$ contributes significantly to $|d\rangle$ [see Fig. 3(c)], however, techniques for phase-stable Raman coupling of hyperfine states are well established [30–32]. The Ω_c beam can be generated using an essentially noise-free passive phase retarder [33], or digital micromirror device [34], and changes in optical path length between the two beams (potentially leading to phase drift) can be interferometrically stabilized if required [35]. Active stabilization techniques [36] can be used in colocating the beams (also with respect to an external trapping potential, if necessary), noting that slightly unequal beam centers and widths (relative to l) do not cause significant qualitative change within the relevant regime of decreasing w. Our GPE treatment ignores quantum fluctuations [10,17]; in the present atom-interferometer context center-of-mass fluctuations are key, effects from which can essentially be avoided in the appropriate velocity regime [14,19,37].

Far from the barrier, we initialize with a soliton in state $|d\rangle \approx |g_1\rangle$. Slow (relative to internal state dynamics) passage across the barrier minimizes coupling to other dressed states; $|d\rangle$ is adiabatically followed, and $|e\rangle$ remains unpopulated, preventing spontaneous decay. This is compatible with the "sudden" passage required for interferometrically desirable high-velocity and narrow-barrier collisions, as we can choose $\Omega \equiv \Omega'(0) = (2/\pi^{1/2})^{1/2}\Omega_0$, setting the time-scale for internal atomic dynamics *independently* from the value of w. It is in principle always possible to set Ω sufficiently high to ensure internal dynamics faster than passage across the barrier. An approximate single-state model, assuming the atoms remain in the internal dark state with spatial profile ψ_d, leads to the scalar GPE

$$i\hbar\frac{\partial\psi_d}{\partial t} = \left(-\frac{\hbar^2}{2m}\frac{\partial^2}{\partial x^2} + V_d + g_{11}^{1D}|\psi_d|^2\right)\psi_d. \tag{4}$$

In the idealized scenario that the scattering lengths a_{jk} are all equal, Eq. (4) applies with $V_d = V_h$, consistent with in this case bright soliton solutions to Eq. (1) existing with spatial density profile independent of the internal state population distribution [38,39]. A more realistic scenario is to tune a_{11} by a Feshbach resonance to a negative value to create bright solitons in state $|g_1\rangle$, where we assume the other scattering lengths are fixed at a background value $a_{jk} = ga_{11}$, in which case

$$V_d(x,|\psi_d|^2) = V_h(x) + (g-1)\frac{2(x/w)^2+1}{[1+(x/w)^2]^2}g_{11}^{1D}|\psi_d|^2, \tag{5}$$

reverting to $V_d = V_h$ when $g = 1$.

We simulate the vector GPE [Eq. (1)] and scalar GPE [Eq. (4)] with periodic boundary conditions, corresponding to a quasi-1D ring trap configuration. We take ^{85}Rb with $|g_1\rangle = |F = 2, M_F - 2\rangle$ and $|g_2\rangle = |F = 2, M_F = 0\rangle$ coupled via the D1 line as an inspirational example. This has a wide Feshbach resonance around $B_0 = 156$ G [40,41], which we use to tune $a_{11} \approx -12\ a_0$, within the stable soliton region [3,42,43]. Assuming all other scattering lengths to be equal to the background value $a_{\rm bg} = -441\ a_0$ yields $g \approx 40$. To broaden our analysis, we vary g between -40 and 40. We work in "soliton" units of length $\hbar^2/m|g_{11}^{1D}|N$, time $\hbar^3/m(g_{11}^{1D}N)^2$, and energy $m(g_{11}^{1D}N/\hbar)^2$ [44]. Unless otherwise stated, we express quantities in these units, with total density normalized to 1. We set $l = 2\sqrt{2}$ in our vector GPE simulations; for the above value of a_{11}, $N = 2500$ and $\omega_r = 2\pi \times 40$ Hz, this corresponds to a metric value of 2.7 μm [19]. We assume an initial bright soliton $\psi_1 = (1/2)\mathrm{sech}([x + L/4]/2)e^{ivx}$ in state $|g_1\rangle$, with $\psi_2 = \psi_e = 0$, and ring trap circumference $L = 64\pi$.

We first use the scalar GPE [Eq. (4)] to investigate soliton collisions with the squared-Lorentzian barrier V_h. We compare the total fraction of transmitted atoms T with the analytic approximation for collisions with a same-height-and-area Rosen-Morse barrier, $V_{\rm RM} = [1/(2w^2)]\mathrm{sech}^2(4x/[\pi w])$, in the high-velocity limit (neglecting the nonlinear term during the collision) [19,45]. We also compare indirectly to scalar GPE simulations with a same-area δ-function barrier, $V_d = V_\delta(x) = [\pi/(4w)]\delta(x)$, which approach their own analytic high-velocity limit

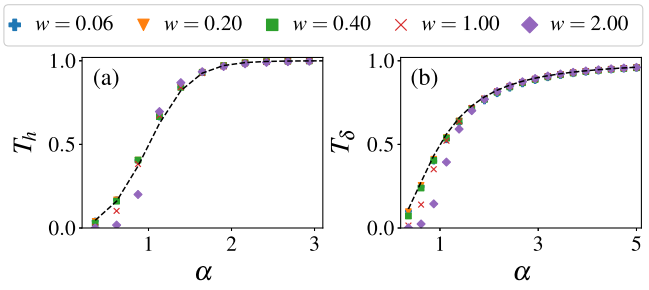

FIG. 2. Bright soliton collisions with the geometric barrier V_h [Eq. (2)] in the scalar GPE [Eq. (4)]. The plots show transmission as a function of α (ratio between velocity and barrier area, in units of $\hbar^{-1}$), for the barriers V_h (a) and V_δ (b), and different values of the width w. Dashed lines in (a) and (b) show high-velocity limits for barriers V_{RM} and V_δ, respectively.

$T_\delta(\alpha) = \alpha^2/(1+\alpha^2)$, where $\alpha = 4vw/\pi$ is the ratio between velocity and barrier area [46]. Figure 2 shows numerical transmission curves for V_h and V_δ barriers with different values of w plotted against α. As w decreases, the transmission curves approach the analytic high-velocity limits for V_{RM} and V_δ. How Figs. 2(a) and 2(b) differ illustrates a key point. Within an interferometer, an effective soliton beam splitter should achieve $T = 0.5$ in the *tunneling regime* (ratio γ between per-atom kinetic energy and barrier height satisfies $\gamma < 1$). The outgoing soliton velocities may otherwise have significantly different magnitudes, as the splitting will increasingly be due simply to reflection of low-velocity and transmission of high-velocity atoms (*velocity filtering* regime) [19]. As collision velocities increase, we need decreasing barrier widths to remain in the tunneling regime [12,37,47]. The V_h barrier width w and area $\pi/(4w)$ are intrinsically inversely related, *fixing* the ratio $\gamma = (vw)^2 = (\pi/4)^2\alpha^2$. Assuming $T = 0.5$ occurs close to $\alpha = 1$, γ tends toward $(\pi/4)^2 \approx 0.61$. The δ-function limit $\gamma \to 0$ is therefore not attained with the V_h barrier; as the width decreases with increasing ratio Ω_1/Ω_0, the velocity at which $T = 0.5$ is nonetheless within the $\gamma < 1$ tunneling regime. In Fig. 3 we investigate these same collisions using the vector GPE description [Eq. (1)] for varying w. We fix incoming soliton velocities at values resulting in $T = 0.5$ for the scalar GPE with $V_d = V_h$ [Fig. 2(a)]. In Figs. 3(a)–3(d) we consider equal scattering lengths ($g = 1$) and characterize internal state populations as functions of time during the collision, showing the integrated time spent in state $|g_2\rangle$ as a function of w in (d). As expected, decreasing w generally reduces the populations of $|g_2\rangle$ and $|e\rangle$ and increases that of $|g_1\rangle$; the integrated time spent in state $|g_2\rangle$ also decreases. In Fig. 3(e) we show the transmission T as a function of w for a range of scattering length ratios g; as w decreases, the effects of $g \neq 1$ reduce. The solid lines in Fig. 3(e) show results of the scalar GPE with fully nonlinear $V_d(x, |\psi_d|^2)$ [Eq. (5)], which clearly matches the vector GPE well over the range of g we explore.

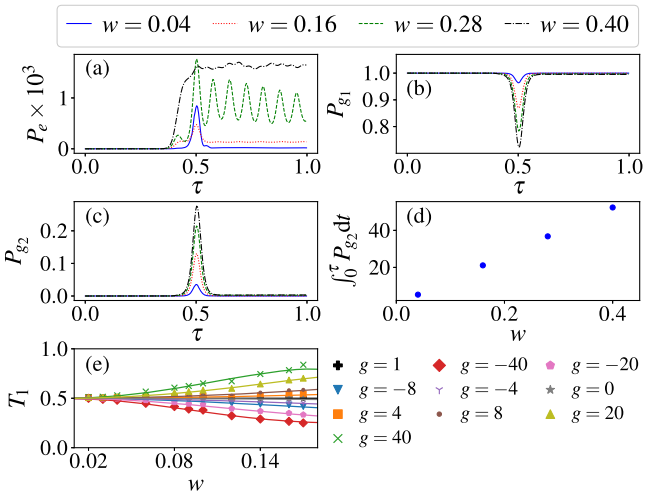

FIG. 3. Bright soliton collisions with the proposed barrier configuration in the vector GPE [Eq. (1)]. (a)–(c) Populations as functions of time (in units of $\tau = L/2v$, the time over which the soliton moves from $-L/4$ to $L/4$) of states $|e\rangle$, $|g_1\rangle$, and $|g_2\rangle$, respectively. (d) Integrated time spent in state $|g_2\rangle$ as a function of w. In (a)–(d), we set $\Omega = 10^4$ and $g = 1$. (e) Transmission as a function of w for different values of g, where we set $\Omega = 10^6$, and fix incoming soliton velocities at values resulting in $T = 0.5$ for scalar GPE simulations with V_h barriers [Fig. 2(a)]; solid lines show equivalent-parameter scalar GPE simulations with fully nonlinear barrier $V_d(x, |\psi_d|^2)$ [Eq. (5)].

While various interferometric configurations are possible, we consider a conceptually simple quasi-1D ring trap with a single barrier. The barrier splits a single soliton into two equal-amplitude, equal-speed counterpropagating daughter solitons, which pass through one another and subsequently phase-sensitively recombine at the same barrier [14]. Imposing a relative phase θ between the daughter solitons, the fraction of atoms recombined to one side of the barrier should vary sinusoidally with θ in the high velocity and narrow barrier limit (i.e., $w \to 0$). We otherwise expect a nonlinearity-induced "skew" in the sinusoidal dependence [11], and employ (generalized) Clausen functions $S_z(\theta)$ to empirically parametrize this effect. We fit the final population on the "transmitted" side of the barrier after the recombination with

$$T_2(\theta) = \frac{1}{2}[1 + AS_z(\theta - \varepsilon)], \tag{6}$$

which ranges from a sawtooth function ($z = 1$) to a sinusoid ($z \to \infty$). To improve fitting convergence and ensure bounded limits, we fit and present results in terms of z^{-1}, where smaller z^{-1} corresponds to less skew [48,49]. The phase shift ε incorporates relative phases accumulated during barrier collisions and subsequent evolution, and A is the contrast or "fringe visibility." For a δ-function barrier in the high-velocity limit $z^{-1} \to 0$, $A = 1$, and $\varepsilon = \pi/2$ [11,46]. In Fig. 4, we show this limit is effectively reached

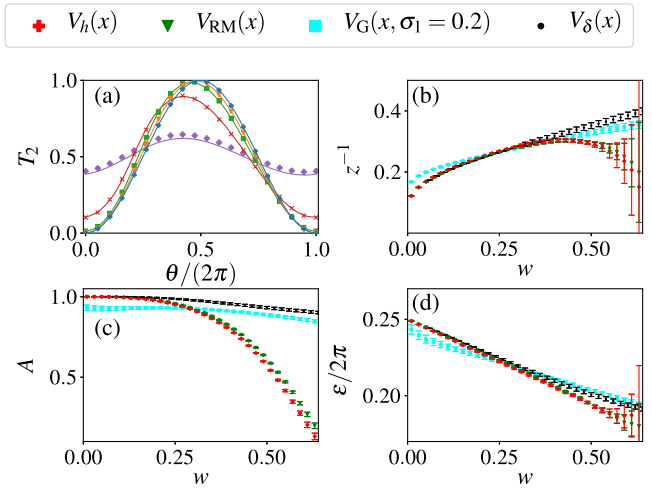

FIG. 4. Bright soliton interferometry with the geometric barrier V_h in the scalar GPE. (a) Transmission at recombination T_2 against imposed phase θ for $w = 0.01$ (blue plus), $w = 0.1$ (orange triangle), $w = 0.2$ (green cross), $w = 0.4$ (red square), and $w = 0.6$ (purple diamond). (b)–(d) Fitted values [using Eq. (6)] of z^{-1}, A, and ε, respectively, for V_h and for the alternative barrier shapes V_{RM}, V_δ, and $V_G(\sigma = 0.2)$ (see text) for varying w.

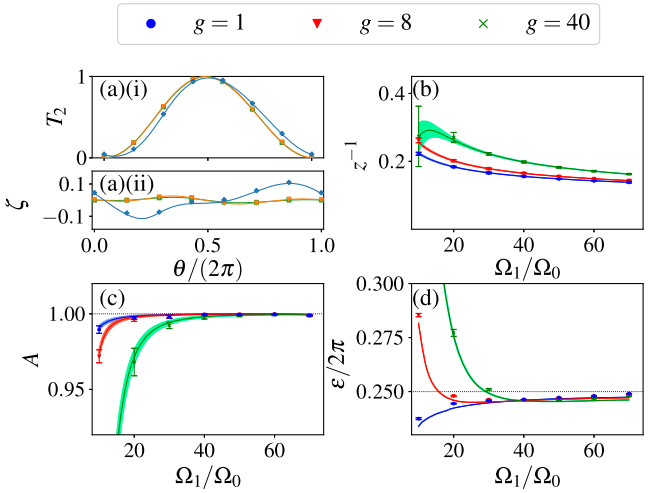

FIG. 5. Bright soliton interferometry in the vector GPE [Eq. (1)]. (a)(i) Transmission at recombination T_2 against imposed phase θ, and (a)(ii) difference from the ideal sinusoid $\zeta = T_2 - (1/2)[1 + \sin(\theta - \pi/2)]$, for $\Omega_1/\Omega_0 = 20$ (blue plus), $\Omega_1/\Omega_0 = 40$ (orange triangle), $\Omega_1/\Omega_0 = 60$ (green square), with $g = 40$. (b)–(d) Values of z^{-1}, A, and ε, respectively, found by fitting with Eq. (6) for $g = 1$, $g = 8$, $g = 40$. Solid lines show the fit to scalar GPE simulations with fully nonlinear barrier $V_d(x, |\psi|^2)$ and equivalent parameters (shaded areas indicate error ranges). We use $\Omega = 10^4$ for $\Omega_1/\Omega_0 = 10$, 20, 30 and $\Omega = 5 \times 10^4$ for $\Omega_1/\Omega_0 = 40$, 50, 60, 70 (see text).

with the V_h barrier in the scalar GPE. We compare this scenario to the scalar GPE with alternative barriers $V_d = V_\delta(x)$, $V_d = V_{\mathrm{RM}}(x)$, and a narrow, fixed-width, Gaussian barrier with equal area to V_h: $V_d = V_G(x;\sigma) = \{[\pi/(4w)]/[(2\pi)^{1/2}\sigma]\}\exp(-x^2/[2\sigma^2])$. For each data point a root-finding algorithm sets the initial velocity to achieve transmission $T = 0.5$ at the first collision, and we model a range of imposed phases θ. Figure 4(a) shows $T_2(\theta)$ for the V_h barrier, directly illustrating the decrease in skew for decreasing w. Figures 4(b)–4(d) show the values of z^{-1}, A, and ε extracted by fitting Eq. (6) to the numerical simulations at width w. The V_h barrier, and its Rosen-Morse approximant V_{RM}, smoothly approach the ideal high-velocity δ-function result of $A = 1$ and $\varepsilon = \pi/2$ as $w \to 0$; note the fixed-width Gaussian barrier performs better at $w \gtrsim 0.3$, but cannot smoothly reach this result. The parameter z^{-1} does not drop smoothly to zero, however at $z^{-1} < 0.2$ the skew is barely resolved and the 3-parameter fit of Eq. (6) effectively overfits in this limit.

In Fig. 5, we analyze the interferometer using the vector GPE [Eq. (1)] for $g = 1$, 8, 40, presenting the results as functions of the ratio $\Omega_1/\Omega_0 \equiv l/(2w)$. Because of the high computational demands of setting the initial velocities with our previously employed root-finding algorithm, we use values determined for Fig. 4 at equivalent widths w for the V_h barrier. In the ideal limit these velocities are the same, but otherwise significantly different A and ε values result for different g. A fully 3D GPE treatment would be even more demanding, however, a 1D treatment captures the essential dynamics within an experimentally reasonable regime [19]. Figure 5(a) shows directly the decrease in skew for $g = 40$ as Ω_1/Ω_0 increases. Figures 5(b)–5(d) show how the fit-extracted parameters z^{-1}, A, and ε tend toward the ideal limit as Ω_1/Ω_0 increases. As in Fig. 3, solid lines show scalar GPE simulations with fully nonlinear potential $V_d(x, |\psi|^2)$ (shaded areas indicate error ranges from fitting), again showing excellent agreement. We require high Ω values to keep internal state dynamics sufficiently fast relative to the collision duration as Ω_1/Ω_0 increases (values used are given in the figure caption). Extension to even higher Ω_1/Ω_0 values is in principle enabled by raising Ω further; the physically desirable strong separation of timescales makes this an increasingly challenging regime to fully simulate, however. Briefly considering off-resonant excitation and spontaneous decay, we similarly note that in the desired regime of operation the splitting at the barrier is a predominantly linear effect [11,46]. Therefore, as an approximate model, we numerically solve the time-independent, three-state linear scattering problem for an incoming plane wave with wave number $k > 0$ in state $|g_1\rangle$, and purely outgoing plane waves in every other channel. We include loss due to spontaneous decay from $|e\rangle$ by combining an imaginary term with the detuning, producing $-\Delta - i\Gamma/2$, where Γ is the excited state linewidth. With ^{85}Rb parameters corresponding to the rightmost points in Figs. 5(b)–5(d), we find the effects of spontaneous decay and realistic detuning (equal to the linewidth) are negligible at the wave number k required for equal splitting [50].

We have described a technique to create a single very narrow barrier for soliton interferometry using a geometric scalar potential [21,22], based on two overlapping Hermite-Gaussian mode laser beams. We used scalar and vector GPE models to characterize the interferometric behavior of this barrier, demonstrating how to realize a very narrow effective barrier using moderately high laser intensity ratios. Critically, the initial equal splitting of a single soliton is then a tunneling rather than a velocity filtering process, and near-unit interferometric contrast is in principle achievable. We have also shown a scalar GPE with correctly chosen nonlinear barrier potential provides an excellent description of the system, provided the intensity of the weaker beam is sufficiently high.

Additional data related to the findings reported in this paper is made available by source [51].

We thank S. L. Cornish, A. Guttridge, I. G. Hughes and A. Rakonjac for useful discussions. C. L. G. is supported by the U.K. EPSRC. This work made use of the Durham University Hamilton HPC Service.

[1] K. E. Strecker, G. B. Partridge, A. G. Truscott, and R. G. Hulet, Formation and propagation of matter-wave soliton trains, Nature (London) **417**, 150 (2002).

[2] L. Khaykovich, F. Schreck, G. Ferrari, T. Bourdel, J. Cubizolles, L. D. Carr, Y. Castin, and C. Salomon, Formation of a matter-wave bright soliton, Science **296**, 1290 (2002).

[3] S. L. Cornish, S. T. Thompson, and C. E. Wieman, Formation of Bright Matter-Wave Solitons during the Collapse of Attractive Bose-Einstein Condensates, Phys. Rev. Lett. **96**, 170401 (2006).

[4] S. Lepoutre, L. Fouché, A. Boissé, G. Berthet, G. Salomon, A. Aspect, and T. Bourdel, Production of strongly bound ^{39}K bright solitons, Phys. Rev. A **94**, 053626 (2016).

[5] T. Mežnaršič, T. Arh, J. Brence, J. Pišljar, K. Gosar, Ž Gosar, R. Žitko, E. Zupanič, and P. Jeglič, Cesium bright matter-wave solitons and soliton trains, Phys. Rev. A **99**, 033625 (2019).

[6] Andrea Di Carli, Craig D. Colquhoun, Grant Henderson, Stuart Flannigan, Gian-Luca Oppo, Andrew J. Daley, Stefan Kuhr, and Elmar Haller, Excitation Modes of Bright Matter-Wave Solitons, Phys. Rev. Lett. **123**, 123602 (2019).

[7] Strictly, such realizations are in the form of bright solitary waves, as the integrability conditions necessary for true solitons are formally not fully satisfied.

[8] N. Veretenov, Yu. Rozhdestvensky, N. Rosanov, V. Smirnov, and S. Federov, Interferometric precision measurements with Bose-Einstein condensate solitons formed by an optical lattice, Eur. Phys. J. D. **42**, 455 (2007).

[9] F. Kh. Abdullaev and V. A. Brazhnyi, Solitons in dipolar Bose-Einstein condensates with a trap and barrier potential, J. Phys. B **45**, 085301 (2012).

[10] A. D. Martin and J. Ruostekoski, Quantum dynamics of atomic bright solitons under splitting and recollision, and implications for interferometry, New J. Phys. **14**, 043040 (2012).

[11] J. L. Helm, T. P. Billam, and S. A. Gardiner, Bright matter-wave soliton collisions at narrow barriers, Phys. Rev. A **85**, 053621 (2012).

[12] J. Polo and V. Ahufinger, Soliton-based matter-wave interferometer, Phys. Rev. A **88**, 053628 (2013).

[13] J. Cuevas, P. G. Kevrekedis, B. A. Malomed, P. Dyke, and R. G. Hulet, Interactions of solitons with a Gaussian barrier: Splitting and recombination in quasi-one-dimensional and three-dimensional settings, New J. Phys. **15**, 063006 (2013).

[14] J. L. Helm, S. L. Cornish, and S. A. Gardiner, Sagnac Interferometry Using Bright Matter-Wave Solitons, Phys. Rev. Lett. **114**, 134101 (2015).

[15] H. Sakaguchi and B. A. Malomed, Matter-wave soliton interferometer based on a nonlinear splitter, New J. Phys. **18**, 025020 (2016).

[16] G. D. McDonald, C. C. N. Kuhn, K. S. Hardman, S. Bennetts, P. J. Everitt, P. A. Altin, J. E. Debs, J. D. Close, and N. P. Robins, Bright Solitonic Matter-Wave Interferometer, Phys. Rev. Lett. **113**, 013002 (2014).

[17] S. A. Haine, Quantum noise in bright soliton matterwave interferometry, New J. Phys. **20**, 033009 (2018).

[18] J. H. V. Nguyen, P. Dyke, D. Luo, B. A. Malomed, and R. G. Hulet, Collisions of matter-wave solitons, Nat. Phys. **10**, 918 (2014).

[19] O. J. Wales, A. Rakonjac, T. P. Billam, J. L. Helm, S. A. Gardiner, and S. L. Cornish, Splitting and recombination of bright-solitary-matter waves, Commun. Phys. **3**, 51 (2020).

[20] A. L. Marchant, T. P. Billam, T. P. Wiles, M. M. H. Yu, S. A. Gardiner, and S. L. Cornish, Controlled formation and reflection of a bright solitary matter-wave, Nat. Commun. **4**, 1865 (2013).

[21] M. Łącki, M. A. Baranov, H. Pichler, and P. Zoller, Nanoscale "Dark State" Optical Potentials for Cold Atoms, Phys. Rev. Lett. **117**, 233001 (2016).

[22] F. Jendrzejewski, S. Eckel, T. G. Tiecke, G. Juzeliūnas, G. K. Campbell, Liang Jiang, and A. V. Gorshkov, Subwavelength-width optical tunnel junctions for ultracold atoms, Phys. Rev. A **94**, 063422 (2016).

[23] R. Dum and M. Olshanii, Gauge Structures in Atom-Laser Interaction: Bloch Oscillations in a Dark Lattice, Phys. Rev. Lett. **76**, 1788 (1996).

[24] N. Goldman, G. Juzeliūnas, P. Öhberg, and I. B. Spielman, Light-induced gauge fields for ultracold atoms, Rep. Prog. Phys. **77**, 126401 (2014).

[25] W. Ge and M. S. Zubairy, Dark-state optical potential barriers with nanoscale spacing, Phys. Rev. A **101**, 023403 (2020).

[26] S. Subhankar, P. Bienias, P. Titum, T.-C. Tsui, Y. Wang, A. V. Gorshkov, S. L. Rolston, and J. V. Porto, Floquet engineering of optical lattices with spatial features and periodicity below the diffraction limit, New J. Phys. **21**, 113058 (2019).

[27] P. Bienias, S. Subhankar, Y. Wang, T.-C. Tsui, F. Jendrzejewski, T. Tiecke, and G. Juzeliūnas, L. Jiang, S. L. Rolston, J. V. Porto, and A. V. Gorshkov, Coherent optical nanotweezers for ultracold atoms, Phys. Rev. A **102**, 013306 (2020).

[28] T-C. Tsui, Y. Wang, S. Subhankar, J. V. Porto, and S. L. Rolston, Realization of a stroboscopic optical lattice for cold atoms with subwavelength spacing, Phys. Rev. A **101**, 041603(R) (2020).
[29] K. T. Kapale and G. S. Agarwal, Subnanoscale resolution for microscopy via coherent population trapping, Opt. Lett. **35**, 2792 (2010).
[30] Yang Zhao, Shaokai Wang, Wei Zhuang, and Tianchu Li, Raman-laser system for absolute gravimeter based on ^{87}Rb atom interferometer, Photonics **7**, 32 (2020).
[31] N. Arias, V. Abediyeh, S. Hamzeloui, and E. Gomez, Low phase noise beams for Raman transitions with a phase modulator and a highly birefringent crystal, Opt. Express **25**, 5290 (2017).
[32] G. Rosi, F. Sorrentino, L. Cacciapuoti, M. Prevedelli, and G. M. Tino, Precision measurement of the Newtonian gravitational constant using cold atoms, Nature (London) **510**, 518 (2014).
[33] T. P. Meyrath, F. Schreck, J. L. Hanssen, C. S. Chuu, and M. G. Raizen, A high frequency optical trap for atoms using Hermite-Gaussian beams, Opt. Express **13**, 2843 (2005).
[34] Philip Zupancic, Philipp M. Preiss, Ruichao Ma, Alexander Lukin, M. Eric Tai, Matthew Rispoli, Rajibul Islam, and Markus Greiner, Ultra-precise holographic beam shaping for microscopic quantum control, Opt. Express **24**, 13881 (2016).
[35] Thomas Uehlinger, Gregor Jotzu, Michael Messer, Daniel Greif, Walter Hofstetter, Ulf Bissbort, and Tilman Esslinger, Artificial Graphene with Tunable Interactions, Phys. Rev. Lett. **111**, 185307 (2013).
[36] R. Gati, M. Albiez, J. Fölling, B. Hemmerling, and M. K. Oberthaler, Realization of a single Josephson junction for Bose-Einstein condensates, Appl. Phys. B **82**, 207 (2006).
[37] J. L. Helm, S. J. Rooney, C. Weiss, and S. A. Gardiner, Splitting bright matter-wave solitons on narrow potential barriers: Quantum to classical transition and applications to interferometry, Phys. Rev. A **89**, 033610 (2014).
[38] B. A. Malomed and R. S. Tasgal, Internal vibrations of a vector soliton in the coupled nonlinear Schrödinger equations, Phys. Rev. E **58**, 2564 (1998).
[39] S. V. Manakov, On the theory of two-dimensional stationary self-focussing of electromagnetic waves, Zh. Eksp. Teor. Fiz. **65**, 505 (1974) [Sov. Phys. JETP **38**, 248 (1974)].
[40] J. L. Roberts, N. R. Claussen, J. P. Burke, C. H. Greene, E. A. Cornell, and C. E. Wieman, Resonant Magnetic Field Control of Elastic Scattering in Cold ^{85}Rb, Phys. Rev. Lett. **81**, 5109 (1998).
[41] C. L. Blackley, C. R Le Sueur, J. M. Hutson, D. J. McCarron, M. P. Köppinger, H.-W. Cho, D. L. Jenkin, and S. L. Cornish, Feshbach resonances in ultracold ^{85}Rb, Phys. Rev. A **87**, 033611 (2013).
[42] P. A. Ruprecht, M. J. Holland, K. Burnett, and M. Edwards, Time-dependent solution of the nonlinear Schrödinger equation for Bose-condensed trapped neutral atoms, Phys. Rev. A **51**, 4704 (1995).
[43] J. L. Roberts, N. R. Claussen, S. L. Cornish, E. A. Donley, E. A. Cornell, and C. E. Wieman, Controlled Collapse of a Bose-Einstein Condensate, Phys. Rev. Lett. **86**, 4211 (2001).
[44] Heuristically this can be expressed as $\hbar = m = |g_{11}^{1D}|N = 1$.
[45] L. D. Landau and E. M. Lifshitz, *Quantum Mechanics (Non-Relativistic Theory)* (Pergamon, New York, 1959).
[46] J. Holmer, J. Marzuola, and M. Zworski, Fast soliton scattering by delta impurities, Commun. Math. Phys. **274**, 187 (2007).
[47] P. Manju, K. S. Hardman, M. A. Sooriyabandara, P. B. Wigley, J. D. Close, N. P. Robins, M. R. Hush, and S. S. Szigeti, Quantum tunneling dynamics of an interacting Bose-Einstein condensate through a Gaussian barrier, Phys. Rev. A **98**, 053629 (2018).
[48] In detail, using `scipy.optimize.curve_fit` [49], we perform a least-squares fit to the numerical T_2 data assuming equal uncertainty in each data point and plot one standard deviation uncertainties in the fit parameters obtained from the covariance matrix after scaling the minimized reduced χ^2 statistic to 1.
[49] P. Virtanen *et al.* (SciPy 1.0 Contributors), SciPy 1.0: Fundamental algorithms for scientific computing in Python, Nat. Methods **17**, 261 (2020).
[50] Specifically, the wave number k required for equal splitting shifts by $\approx 2\%$, and $\approx 2\%$ of the incoming atom flux is lost at this wave number. Multiplying this proportion by 356.86 nK [the ^{85}Rb D_1 recoil temperature (https://steck.us/alkalidata/rubidium85numbers.pdf)] corresponds to an approximate overall temperature increase of just 7.14 nK.
[51] Callum L. Grimshaw, Data are available through Durham University data management, 2021, http://doi.org/10.15128/r11j92g749r.